Supporting information

Deciphering Anomalous Zinc Ions Storage in Intermediate State MnO$_2$ of Layer-to-Tunnel Transition

Xiaohui Li[a†], Dayin He[b†], Qiancheng Zhou[a], Xing Zhou[c], Zhouzhou Wang[a], Chenchen Wei[a], Yaran Shi[a], Xiyang Hu[a], Bangwang Huang[a], Ze Yang[a*], Xiao Han[b*], Yue Lin[b], and Ying Yu[a*]

[†] Contributed equally to this work.

[a] Institute of Nanoscience and Nanotechnology, College of Physical Science and Technology, Central China Normal University, Wuhan, 430079, China.

[b] Hefei National Research Center for Physical Sciences at the Microscale, University of Science and Technology of China, Hefei, 230026 China.

[c] State Key Laboratory of Advanced Technology for Materials Synthesis and processing Wuhan University of Technology, Wuhan 430070, China.

*E-mails: yz@ccnu.edu.cn (Z. Yang);

xhan@ustc.edu.cn (X. Han);

yuying01@ccnu.edu.cn (Y. Yu)

Experimental Section

Synthesis various structures MnO$_2$: Solution A was obtained by dissolving 1.5 mmol KMnO$_4$ in 50 mL DI H$_2$O; 1 mmol MnSO$_4$•H$_2$O was dissolved in 25 mL DI H$_2$O to obtain solution B; Solution B was poured into solution A, then the evenly mixed solution was placed in 100 mL Teflon-lined stainless-steel autoclave and hydrothermal reaction at 120 °C for 6 h. The IS-MnO$_2$ powders were collected by centrifugation and dried at 60 °C for 12 h. δ-MnO$_2$ and α-MnO$_2$ were prepared by controlling the hydrothermal reaction time (3 h and 9 h) using the same experimental method.

Assemble Zn//MnO$_2$ coin cell: The pre-prepared MnO$_2$ powders were mixed with acetylene black and PVDF according to the mass ratio 7:2:1 and stirred with appropriate amount of N-methyl pyrrolidone solvent for 6 h to obtain the slurry. Finally, the slurry was coated on the Ti foil and dried in vacuum at 60 °C for 12 h to obtain MnO$_2$ cathode. Zn//MnO$_2$ coin cell (CR2032) were assembled with various structure MnO$_2$ as the cathode (d = 12 mm, the active material loading is about 1.5 ~ 2 mg), Zn foil (50 μm) as the anode, 2 M ZnSO$_4$ + 0.1 M MnSO$_4$ aqueous solution as the electrolyte, and glass fiber (GF/D, Whatman) as the separator in air atmosphere.

Characterization: The morphology and microstructure of various MnO$_2$ samples were observed by field-emission scanning electron microscopy (SEM, JEOLJSM-7900F), transmission electron microscopy (TEM, Titan G260-300 with a probe corrector) and high-angle annular dark-field scanning transmission electron microscope (HAADF-STEM, JEOL ARM200F). X-ray diffractometer (XRD,

PANalytical X'PertPRO, Cu Kα radiation), X-ray pair distribution function (PDF, Bruker D8 ADVANCE, Ag Kα radiation), Raman spectroscopy (LabRAM HR JYEvolution, 532 nm), X-ray photoelectron spectroscopy (XPS, EscaLab 250Xi) and electron energy loss spectroscopy (EELS) were used to analyze the chemical composition, structure, phase change, and valence state of samples. X-ray absorption spectroscopy (XAS) spectra of Mn K-edge were carried out at the X-ray absorption station (beamline 1W2B) of the Beijing Synchrotron Radiation Facility (BSRF). *In-situ* XRD (XRD, Bruker D8 ADVANCE, Cu Kα radiation) was used to investigate the structure change of IS MnO_2 during the charging and discharging.

Electrochemical measurements: The cyclic voltammetry (CV) curves and electrochemical impedance spectrum (EIS) of cells were measured by CHI760E electrochemistry workstation. CV curves are obtained at various scanning rate in a voltage window of 0.8 - 1.85 V. The frequency range of EIS is $1\text{-}10^5$ Hz. The galvanostatic charge/discharge (GCD) curves, rate performance, cycle performance and galvanostatic intermittent titration technique (GITT) tests were measured in the Neware battery test system.

DFT details: The DFT calculations were performed using the Vienna Ab initio Simulation Package. The projector-augmented wave (PAW) method was applied to deal with the ion-electron interactions. The generalized gradient approximation (GGA) with Perdew-Burke-Ernzerhof (PBE) functional was used. The cut off energy was set to 500 eV, and the spin of the system is considered. The models of layered, tunnel and mixed-phase MnO_2 each consist of 8 MnO_2 units. Different densities of k-points were

employed in computing their DOS due to variations in the cell shape: 9×9×3, 4×11×2, and 3×3×11, respectively. In all calculations related to DOS, the presence of K ions has not been considered, and the valence electron count of the system has not been altered. In order to ensure that the computed DOS curves have similar precision, the number of sampling points was increased by setting NEDOS=3000 in the calculations.

The models used in this study to simulate three types of manganese dioxide exhibit a layered, tunnel, and intermediate structure, respectively. Each manganese dioxide model contains 16 manganese (Mn) atoms and 32 oxygen (O) atoms, resulting in a total of 16 manganese dioxide units. This consistency in the number of manganese dioxide units allows for meaningful comparison of the energy changes during the zinc ion embedding processes. The layered manganese dioxide model consists of four layers. To better simulate realistic reaction environments, we initially embedded a potassium ion and successively embedded one, two, and three zinc ions. We then compared the energy changes during these processes. Similar procedures were applied to the intermediate and tunnel models. The detailed coordinate information for the three manganese dioxide models and top-down views depicting the embedding of varying numbers of zinc ions will be provided below. The energy of the Zn ion is taken to be the chemical potential (μ_{Zn}) of a single Zn atom. In the energy profile, the energy change at each step represents the difference between the structure's energy after embedding the Zn atom and the energy of the unembedded zinc ion. For example, the energy difference between the state of embedding two zinc atoms and the state of embedding one zinc atom is given by $E_2 - E_1 - \mu_{Zn}$, where E_2

and E_1 are the energies after embedding two and one zinc atoms, respectively, and μ_{Zn} is the chemical potential of a single Zn atom.
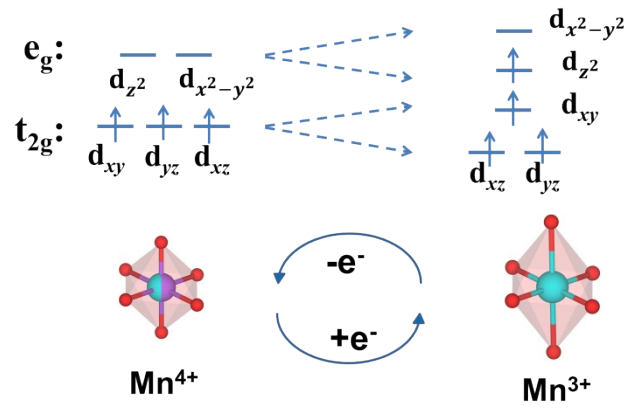
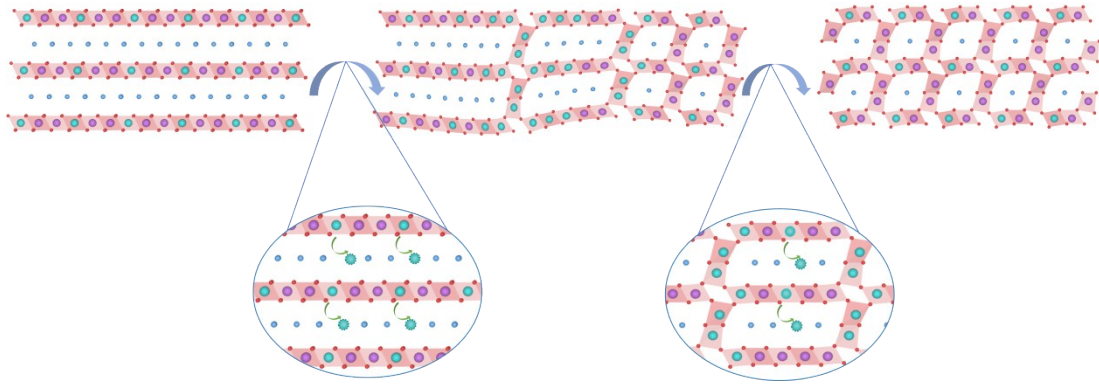Figure S1. Schematic diagram of MnO_2 J-T effect.

Figure S2. Schematic diagrams of the transition from layered to tunnel MnO_2.
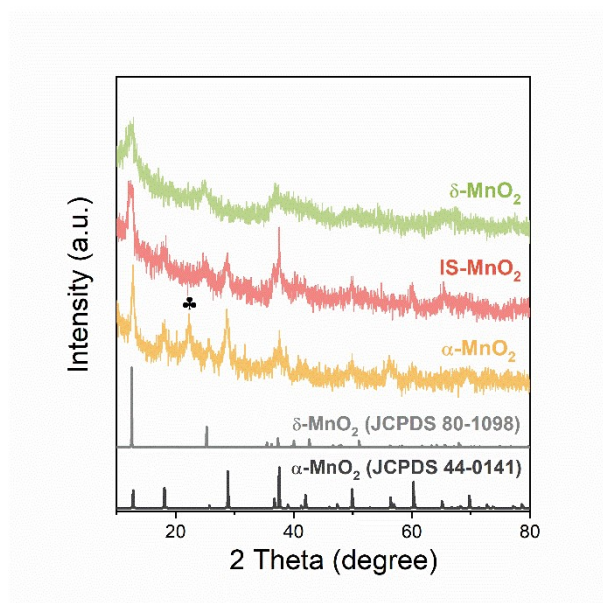
Figure S3. XRD patterns of δ-MnO_2, IS-MnO_2 and α-MnO_2.

There are γ-phase MnO_2 diffraction peaks (marked diffraction peaks at about 23°) in the XRD results of α-MnO_2, which is due to the possible formation of a small number of [1*2] tunnels during the phase transition process.
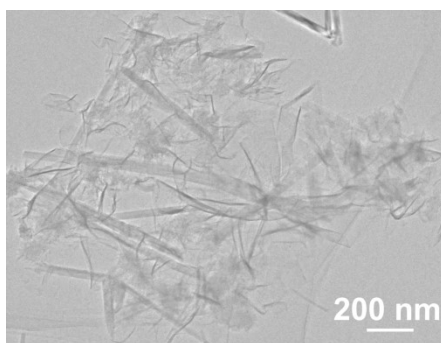
Figure S4. TEM image of IS-MnO$_2$.
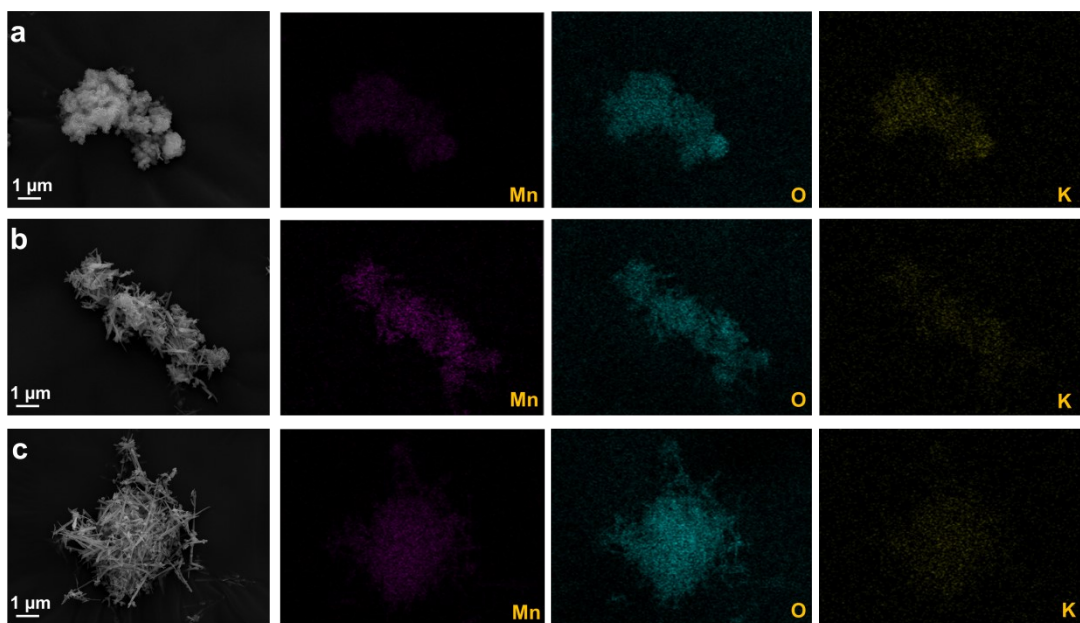
Figure S5. SEM images and corresponding EDS element mapping of (a) δ-MnO$_2$, (b) IS-MnO$_2$, and (c) α-MnO$_2$.
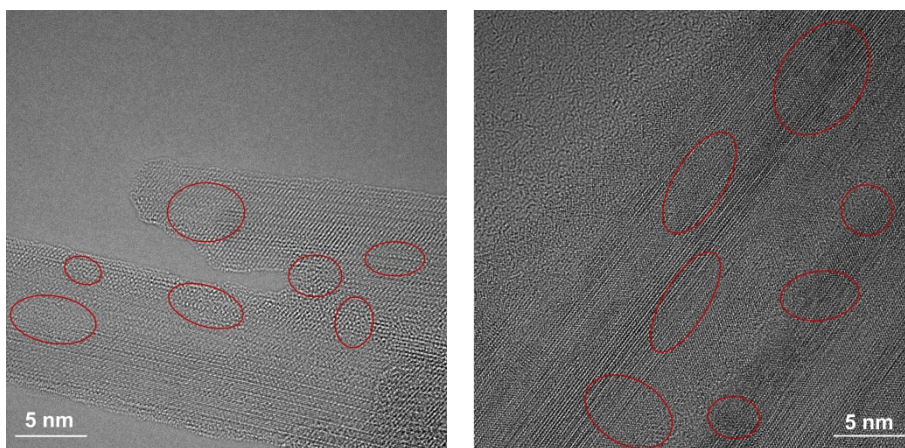
Figure S6. HRTEM images of two random positions in IS-MnO$_2$. (Regions marked in red are the structural transition zones.)
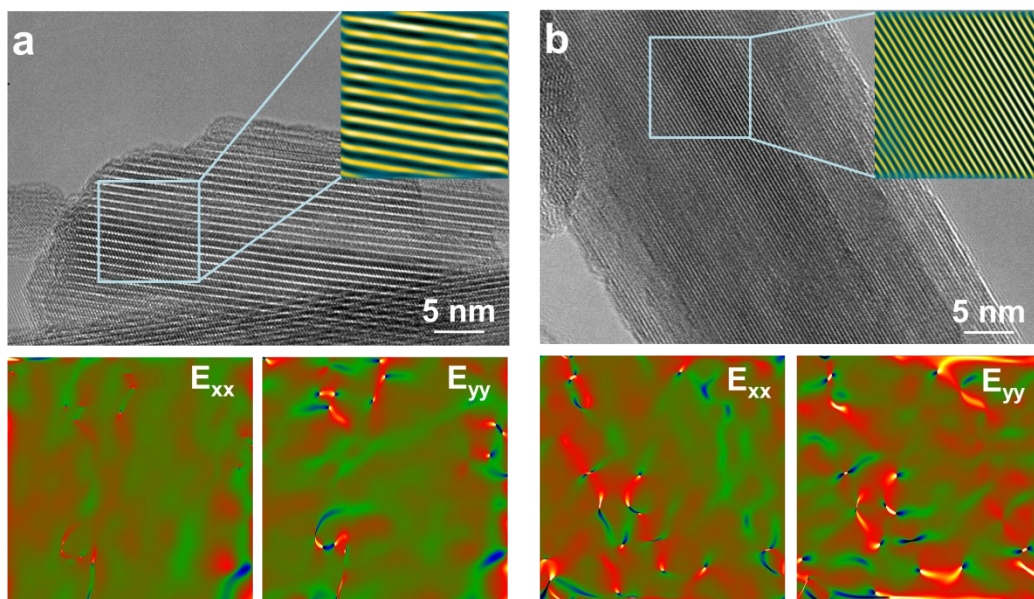
Figure S7. TEM images and GPA strain maps of (a) δ-MnO$_2$ and (b) α-MnO$_2$.
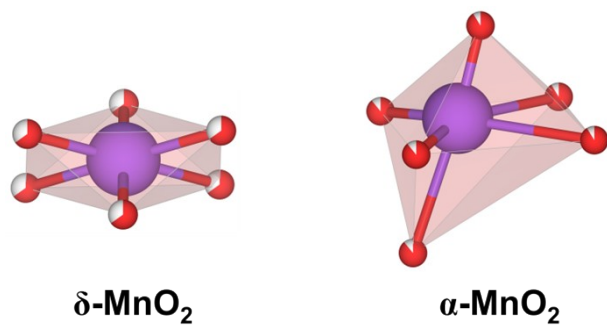
δ-MnO₂　　**α-MnO₂**

Figure S8. Refined structure model of δ and α phase in IS-MnO$_2$.
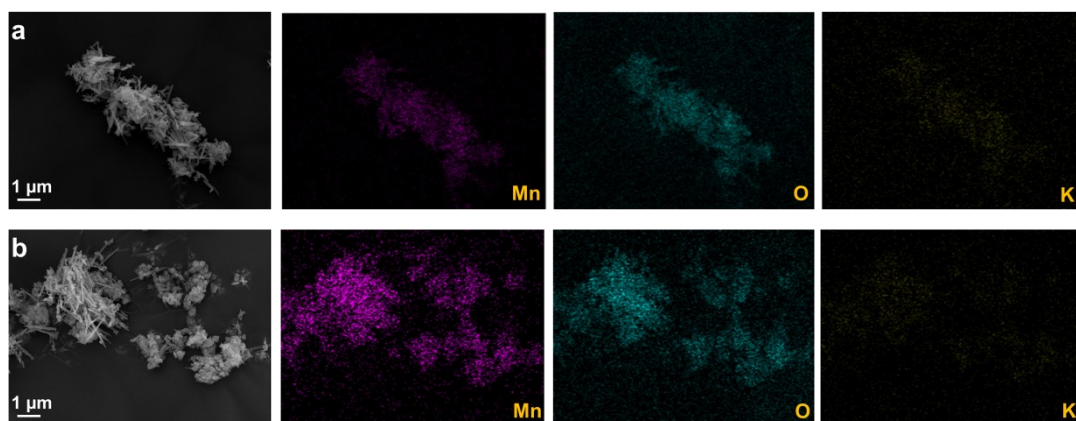
Figure S9. SEM images and corresponding EDS element mapping of (a) IS-MnO$_2$ and (b) α+δ-MnO$_2$.
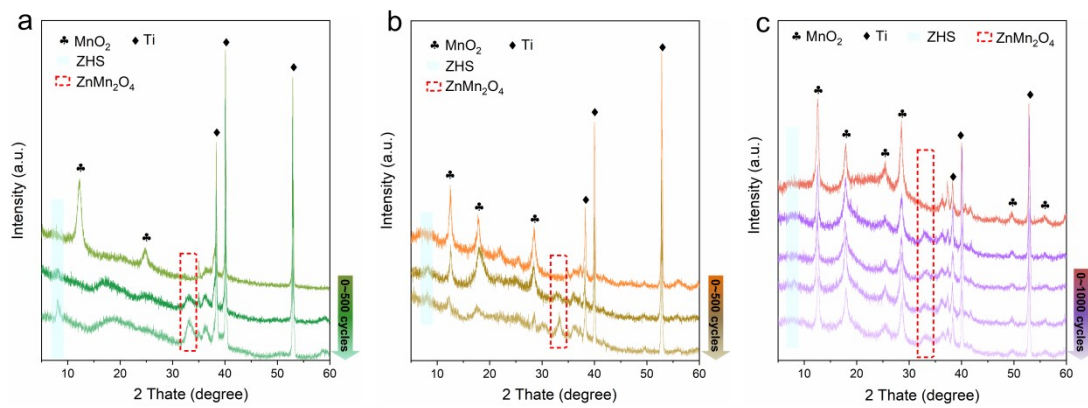
Figure S10. XRD patterns of (a) δ-MnO$_2$, (b) α-MnO$_2$ and (c) IS-MnO$_2$ cathode with full charge state in various cycles.
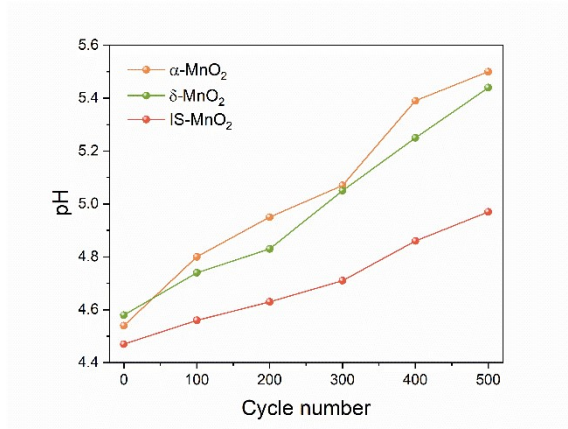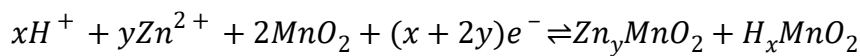
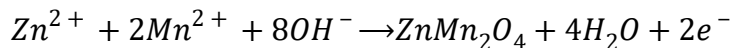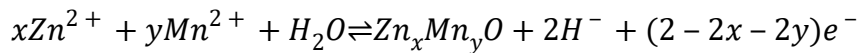Figure S11. pH monitoring of δ-MnO$_2$, α-MnO$_2$ and IS-MnO$_2$ cathode in various cycles.

MnO$_2$ cathode reaction mechanism in Mn^{2+}-containing electrolyte can be summarized as:

1) H$^+$/Zn^{2+}-dominated intercalation reactions;

$$xH^+ + yZn^{2+} + 2MnO_2 + (x + 2y)e^- \rightleftharpoons Zn_yMnO_2 + H_xMnO_2$$

2) Mn^{2+}-dominated deposition reactions.

$$xZn^{2+} + yMn^{2+} + H_2O \rightleftharpoons Zn_xMn_yO + 2H^- + (2 - 2x - 2y)e^-$$

$$Zn^{2+} + 2Mn^{2+} + 8OH^- \longrightarrow ZnMn_2O_4 + 4H_2O + 2e^-$$

As shown in Figure S11, the electrolyte pH value of δ-MnO$_2$ and α-MnO$_2$ cathode increased rapidly during cycling, which means that the H$^+$ ions are heavily consumed. The H$^+$ ion consumption of cathode mainly origins from the J-T effect triggered by H$^+$/Zn^{2+} ion intercalation reaction, which leads to the destruction of electrode structure, and the intercalation reaction becomes not completely reversible. The sharp rise of pH value further promotes the deposition reaction of Mn^{2+} ions, aggravates the production of dead "Mn" (ZnMn$_2$O$_4$), and eventually leads to the failure of capacity. In contrast, the slow increase of electrolyte pH value for IS-MnO$_2$

indicates that the ions intercalation reaction of the cathode is more reversible, leading

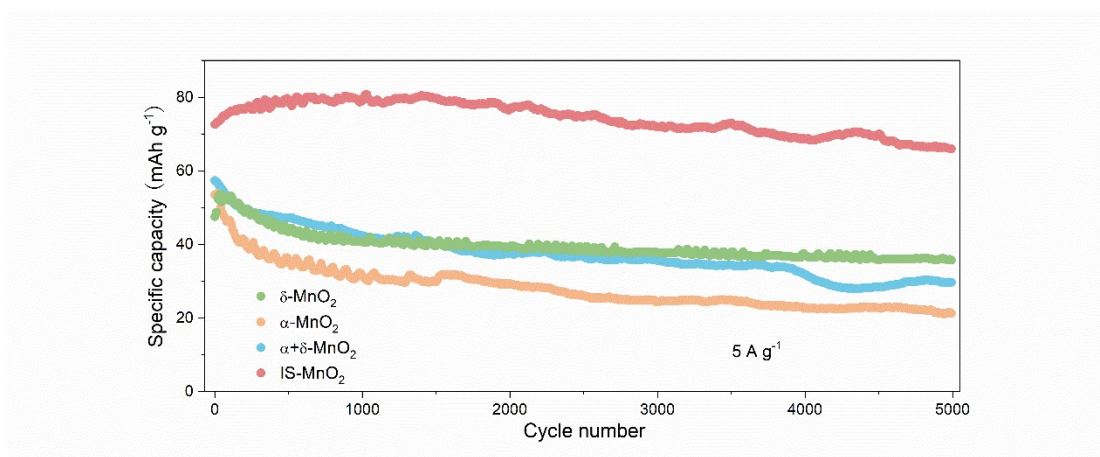to that fact that the structure is more stable, and the J-T effect is inhibited.

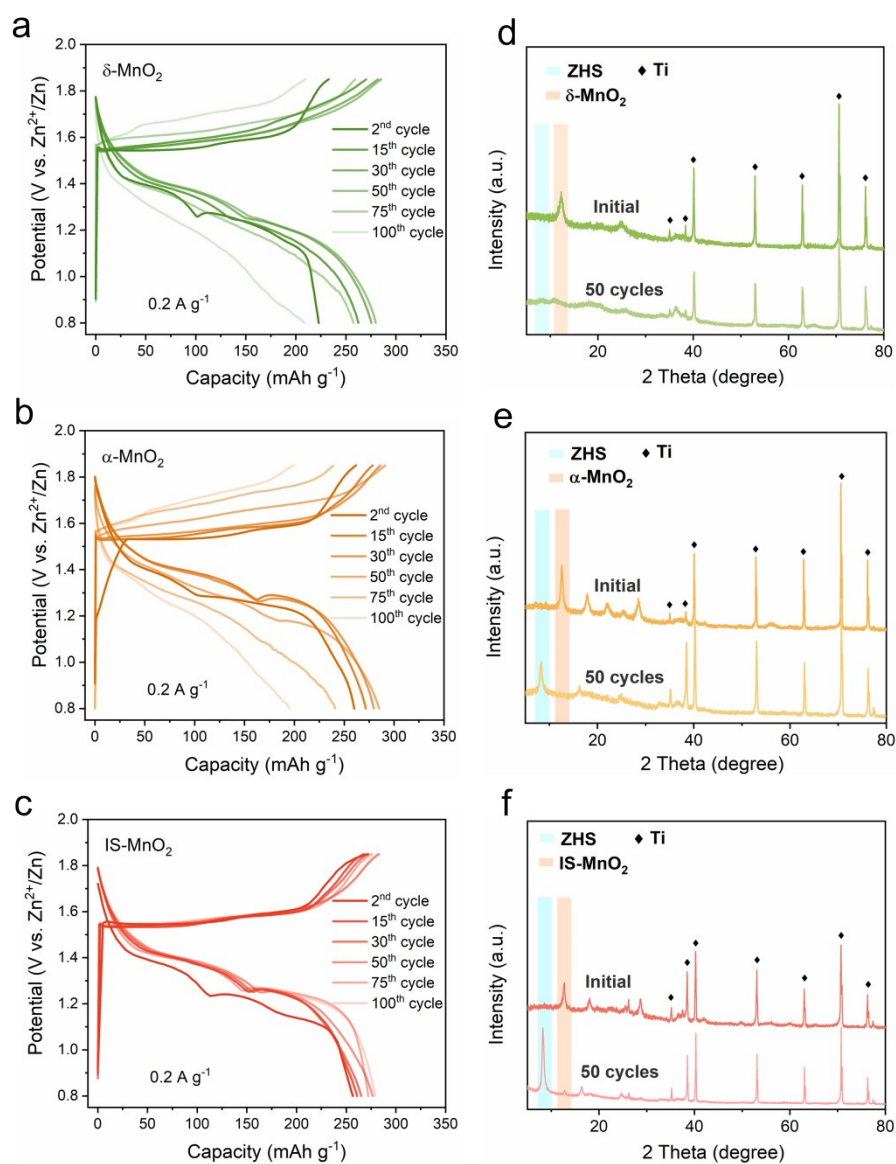Figure S12. Long cyclic performances of α-MnO$_2$, δ-MnO$_2$, α+δ-MnO$_2$ and IS-MnO$_2$ cathodes at 5 A g^{-1}.

Figure S13. GCD curves of (a) δ-MnO₂, (b) α-MnO₂, (c) IS-MnO₂ at various cycles.

XRD patterns of (d) δ-MnO₂, (e) α-MnO₂, (f) IS-MnO₂ before and after cycles.
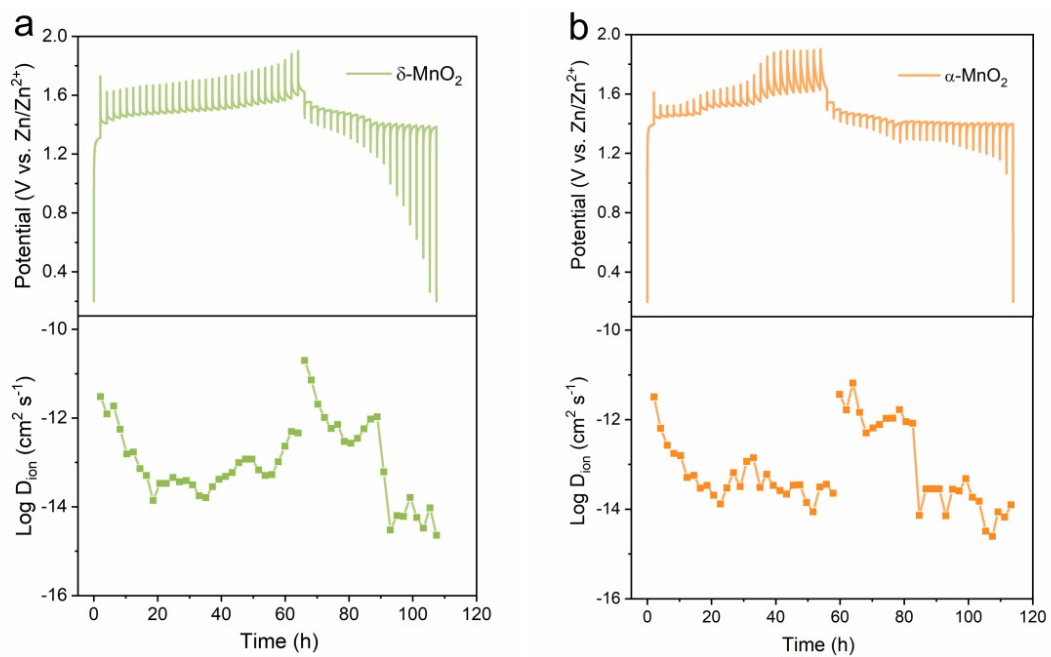
Figure S14. GITT curves and the corresponding Zn^{2+} ion diffusion coefficients of (a) δ-MnO$_2$, (b) α-MnO$_2$.
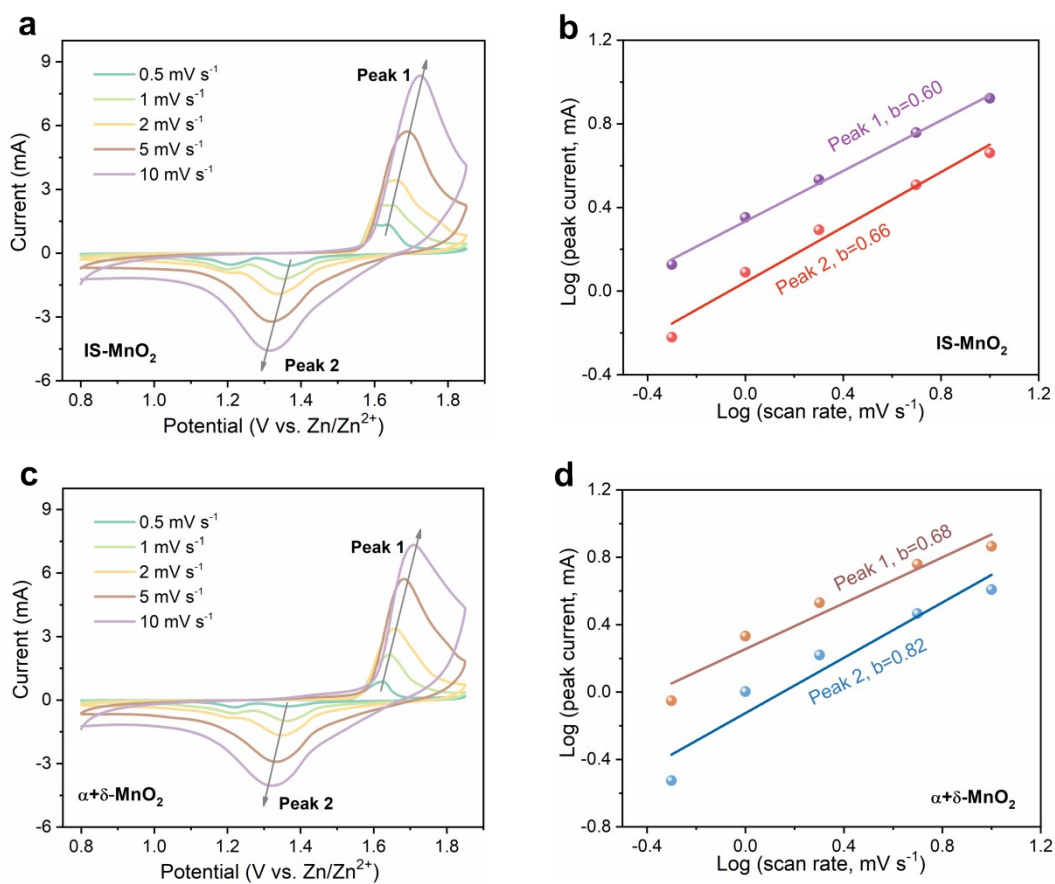
Figure S15. CV curves at various scan rates and Log(i) vs. Log(v) plots of peaks in CV curves of (a, b) IS-MnO$_2$ and (c, d) α+δ-MnO$_2$.
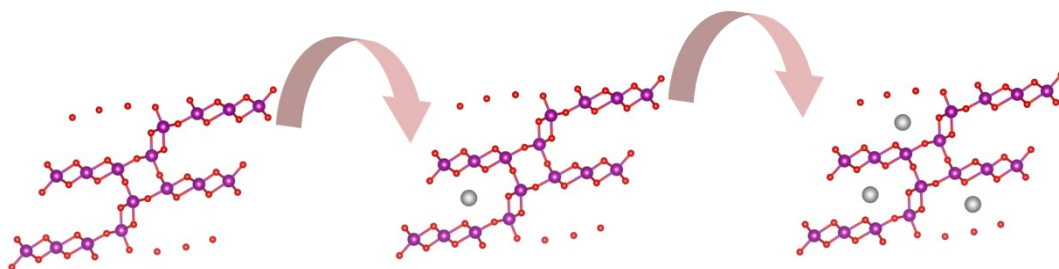
Figure S16. Schematic diagram of ions inserting into IS-MnO$_2$.
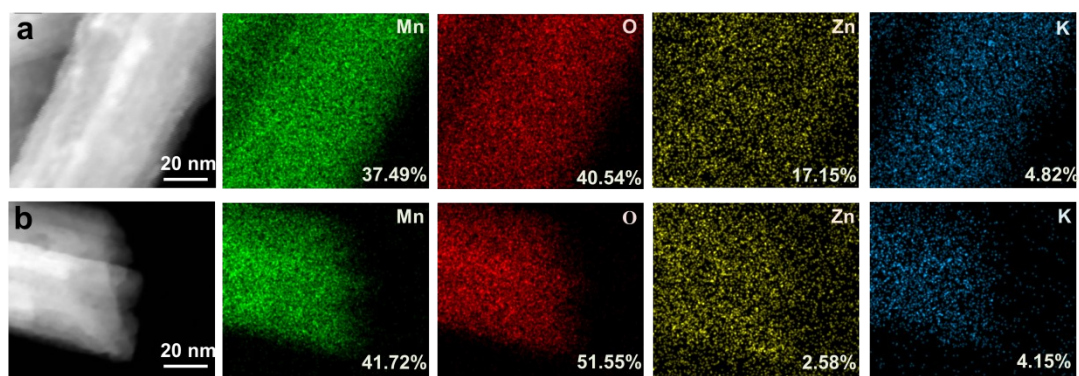
Figure S17. HAADF-STEM images and corresponding EDS element mapping of IS-MnO$_2$ at (a) full discharge state and (b) full charge state.
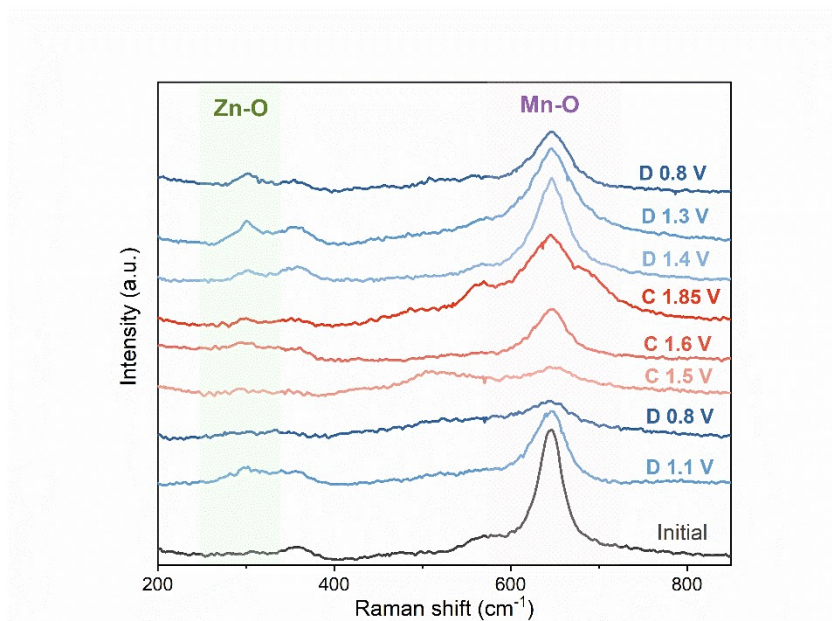
Figure S18. *Ex-situ* Raman spectra of IS-MnO$_2$ at specific voltage states.
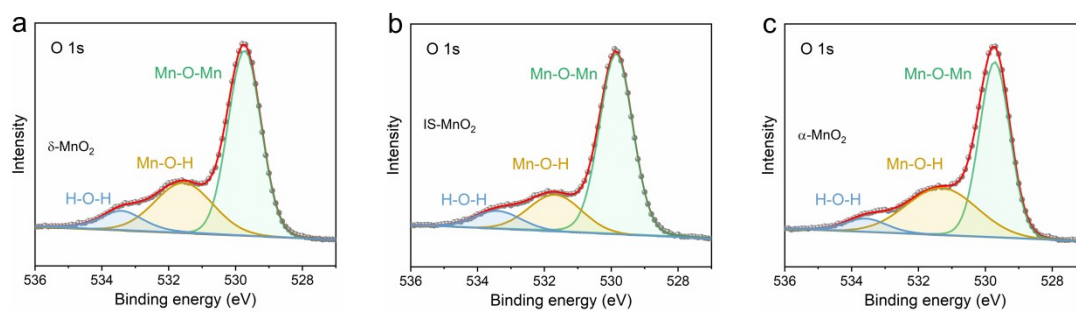
Figure S19. O 1s XPS spectra of (a) δ-MnO$_2$, (b) IS-MnO$_2$, (c) α-MnO$_2$.

δ-MnO$_2$ α-MnO$_2$
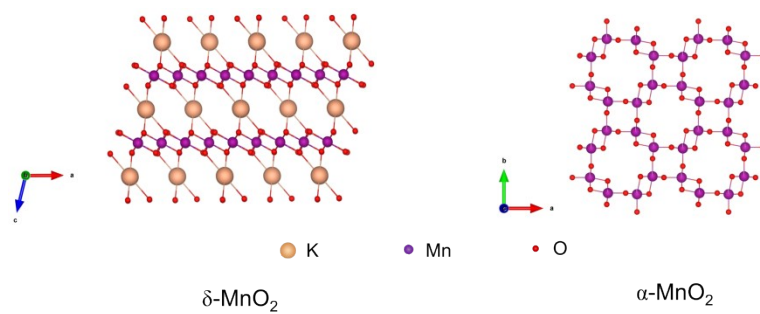
Figure S20. Standard model in X-ray PDF.
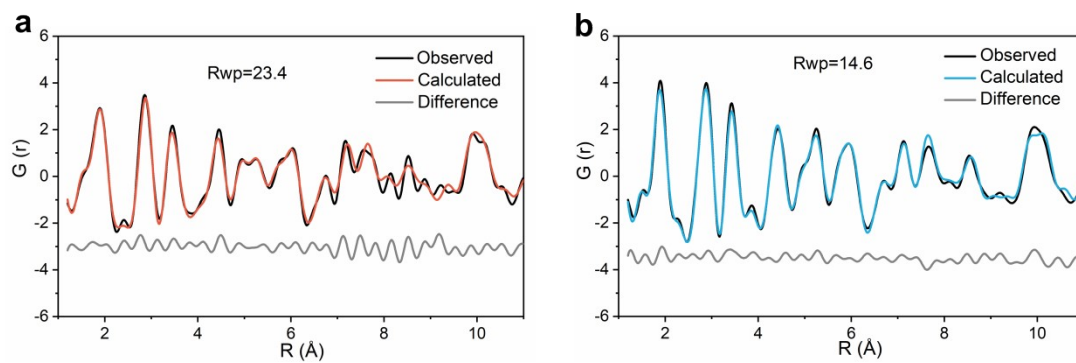
Figure S21. Refinement X-ray PDF patterns of (a) IS-MnO$_2$ and (b) α+δ-MnO$_2$.
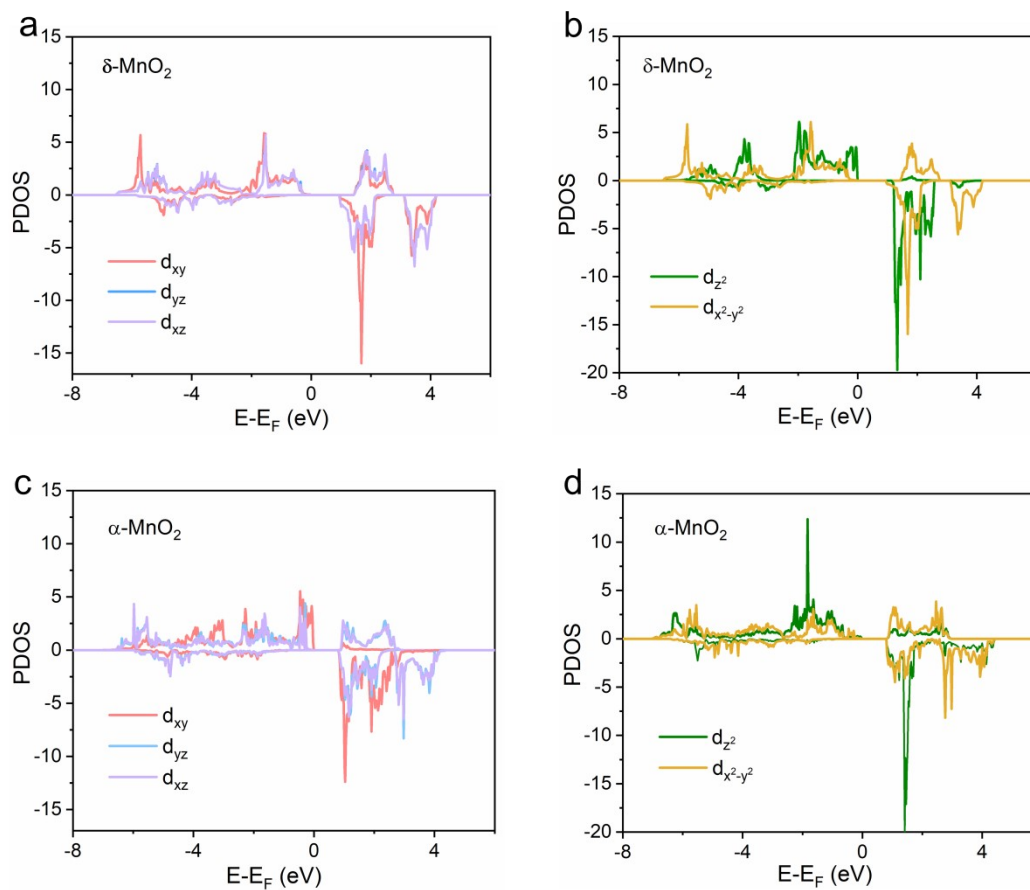
Figure S22. Partial density of states of t_{2g} and e_g orbits in (a, b) δ-MnO$_2$ and (c, d) α-MnO$_2$.
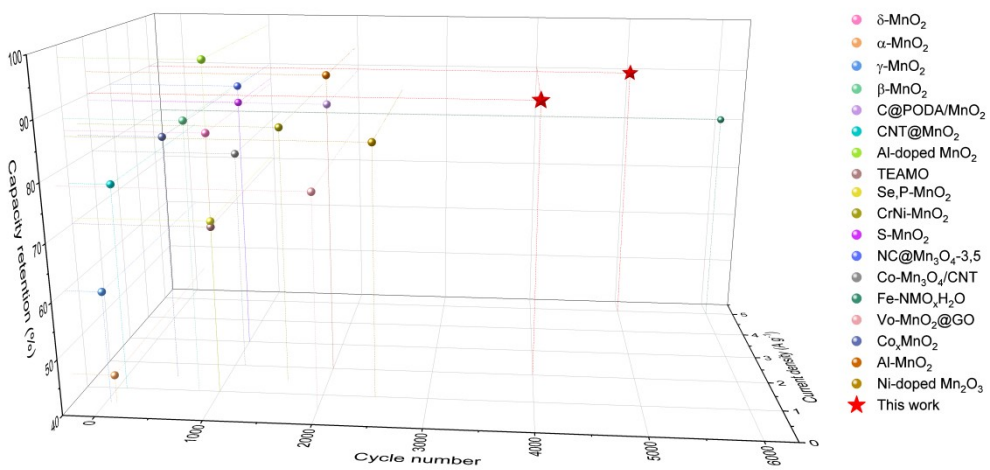
Figure S23. Performance comparison with other reported Mn-based cathode.

Table S1. Lattice parameters of the refined δ phase in IS MnO$_2$.

Space group	a/Å	b/Å	c/Å	α(°)	β(°)	γ(°)
C 2/m (12)	4.92655	2.88846	7.2191	90	97.39	90

Table S2. Atom occupation of the refined δ phase in IS MnO$_2$.

Number	Atom	x	y	z	Occupation
1	Mn	0	0	0	1
2	O	0.352	0	0.076	0.654
3	K	0.926	0.5	0.421	0.305

Table S3. Lattice parameters of the refined of the refined α phase in IS MnO$_2$.

Space group	a/Å	b/Å	c/Å	α(°)	β(°)	γ(°)
I 4/m (87)	9.81815	9.81815	2.85375	90	90	90

Table S4. Atom occupation of the refined α phase in IS MnO$_2$.

Number	Atom	x	y	z	Occupation
1	Mn	0.339	0.152	0	1
2	O	0.188	0.159	0	0.91
3	O	0.563	0.123	0	0.889
4	K	0	0	0.5	0.435

Table S5. Proportion of various valences Mn in various samples.

Samples	Mn^{4+}	Mn^{3+}	Mn^{2+}
IS- MnO_2	43%	49%	8%
δ-MnO_2	48%	46%	6%
α-MnO_2	55%	42%	3%

Table S6. Mn K-edge EXAFS fitting parameters in various samples.

Samples	Path	CN	R (Å)	σ^2	R factor
	Mn-O	5.4	1.89	0.004	
IS-MnO_2	Mn-Mn$_{edge}$	5.2	2.48	0.007	0.0102
	Mn-Mn$_{corner}$	5.1	2.89	0.006	
	Mn-O	5.7	1.90	0.003	
α+δ MnO_2	Mn-Mn$_{edge}$	5.8	2.44	0.006	0.0058
	Mn-Mn$_{corner}$	3.5	2.88	0.004	

CN is the coordination number; R is distance between absorber and backscatter atoms; σ^2 is Debye-Waller factor (represents the thermal and static disorder in absorber-scatterer distances); R factor is used to assess the goodness of the fitting.

Table S7. Grain radius in various samples.

samples	δ phase	α phase
IS-MnO$_2$	22.25 Å	11.66 Å
α+δ-MnO$_2$	135.58 Å	46.47 Å

Table S8. Performance comparison of MnO_2 cathode with those in reported literatures.

Samples	Current density (A g^{-1})	Capacity (mAh g^{-1})	Cycle number	Capacity retention
δ-MnO$_2$[1]	1	177	1000	86%
α-MnO$_2$[2]	0.5	200	100	45%
γ-MnO$_2$[3]	0.5	219	45	60%
β-MnO$_2$[4]	1	171	800	88%
C@PODA/MnO$_2$[5]	2	137	2000	89%
CNT@MnO$_2$[6]	1	92	90	77%
Al-doped MnO$_2$[7]	1	201	1000	98%
TEAMO[8]	1	180	1000	70%
Se, P-MnO$_2$[9]	1	232	1000	71%
CrNi-MnO$_2$[10]	1.5	192	1600	86%
S-MnO$_2$[11]	3	150	1000	87%
NC@Mn$_3$O$_4$-3,5[12]	3	267	1000	90%
Co-Mn$_3$O$_4$/CNA[13]	2	150	1100	80%
Fe-NMO$_x$H$_2$O[14]	5	95	6000	81%
V$_O$-MnO$_2$@GO[15]	1.5	130	2000	78%
CoxMnO$_2$[16]	0.5	100	500	84%
Al-MnO$_2$[17]	2	275	2000	94%
Ni-doped Mn$_2$O$_3$[18]	1	132	2500	85%
This work	2	160	4000	90.3%

5	**90**	**5000**	**90.0%**

Reference

[1] H. Tang, W. Chen, N. Li, Z. Hu, L. Xiao, Y. Xie, L. Xi, L. Ni and Y. Zhu, *Energy Storage Materials*, 2022, **48**, 335-343.

[2] X. Gao, H. Wu, W. Li, Y. Tian, Y. Zhang, H. Wu, L. Yang, G. Zou, H. Hou and X. Ji, *Small*, 2020, **16**, 1905842.

[3] M. H. Alfaruqi, V. Mathew, J. Gim, S. Kim, J. Song, J. P. Baboo, S. H. Choi and J. Kim, *Chemistry of Materials*, 2015, **27**, 3609-3620.

[4] J. Zheng, C. Qin, C. Chen, C. Zhang, P. Shi, X. Chen, Y. Gan, J. Li, J. Yao, X. Liu, J. Cheng, D. Sun, H. Wan and H. Wang, *Journal of Materials Chemistry A*, 2023,**11**, 24311-24320.

[5] Y. Zhao, R. Zhou, Z. Song, X. Zhang, T. Zhang, A. Zhou, F. Wu, R. Chen, and L. Li, *Angewandte Chemie International Edition*, 2022, **61**, e202212231.

[6] Y. Ren, F. Meng, S. Zhang, B. Ping, H. Li, B. Yin and T. Ma, *Carbon Energy*, 2022, **4**, 446-457.

[7] Y. Zhao, S. Zhang, Y. Zhang, J. Liang, L. Ren, H. J. Fan, W. Liu and X. Sun, *Energy & Environmental Science*, 2024, **17**, 1279-1290.

[8] S. Wang, S. Yao, N. Dai, W. Fu, Y. Liu, K. Ji, Yi. Ji, J. Yang, R. Liu, X. Li, J. Xie, Z. Yang and Y. M. Yan, *Angewandte Chemie International Edition*, 2024, doi.org/10.1002/anie.202408414.

[9] K. Ma, S. Ge, R. Fu, C. Feng, H. Zhao, X. Shen, G. Liang, Y. Zhao and Q. Jiao, *Chemical Engineering Journal*, 2024, **484**, 149525.

[10] Y. Zhao, X. Xia, Q. Li, Y. Wang, Y. Fan, Y. Zhao, W. Li and X. Sun, *Energy Storage Materials*, 2024, **67**, 103268.

[11] Y. Zhao, P. Zhang, J. Liang, X. Xia, L. Ren, L. Song, W. Liu, X. Sun, *Energy Storage Materials*, 2022, **47**, 424-433.

[12] M. Xie, X. Zhang, R. Wang, Y. Jiao, Z. Shu, S. Shan , Y. Bian, H. Lin, J. Chen, and Y. Xu, *Chemical Engineering Journal*, 2024, **494**, 152908.

[13] J. Ji, H. Wan, B. Zhang, C. Wang, Y. Gan, Q. Tan, N. Wang, J. Yao, Z. Zheng, P. Liang,

J. Zhang, H. Wang, L. Tao, Y. Wang, D. Chao, and H. Wang, *Advanced Energy Materials*, 2021, **11**, 2003203.

[14] X. Li, Y. Sun, L. Zhou, H. Wang, B. Xie, W. Lu, J. Ning and Y. Hu, *Materials Horizons*, 2024, 10.1039/d4mh00544a.

[15] S. Ding, M. Zhang, R. Qin, J. Fang, H. Ren, H. Yi, L. Liu, W. Zhao, Y. Li, L. Yao, S. Li, Q. Zhao and F. Pan, *Nano-Micro Letters*, 2021, **13**, 173.

[16] Q. Chen, X. Lou, Y. Yuan, K. You, C. Li, C. Jiang, Y. Zeng, S. Zhou, J. Zhang, G. Hou, J. Lu and Y. Tang, *Advanced Materials*, 2023, **35**, 2306294.

[17] C. Chen, M. Shi, Y. Zhao, C. Yang, L. Zhao and C. Yan, *Chemical Engineering Journal*, 2021, **422**, 130375.

[18] D. Zhang, J. Cao, X. Zhang, N. Insin, S. Wang, J. Han,Y. Zhao, J. Qin and Y. Huang, *Advanced Functional Materials*, 2021, **31**, 2009412.